PAPER • **OPEN ACCESS**

Charge transport and charge trapping in polycrystalline ZnO thin films doped by methane: local and integrated analysis

To cite this article: Y V Gomeniuk *et al* 2025 *Phys. Scr.* **100** 025905

Physica Scripta

PAPER

Charge transport and charge trapping in polycrystalline ZnO thin films doped by methane: local and integrated analysis

Y V Gomeniuk[1,*], **P M Lytvyn**[1], **Y Y Gomeniuk**[1], **T E Rudenko**[1], **A V Vasin**[1], **A V Rusavsky**[1], **V S Lysenko**[1], **V Kilchytska**[2], **D Flandre**[2] **and A N Nazarov**[1,3]

[1] Lashkaryov Institute of Semiconductor Physics, National Academy of Sciences of Ukraine, 41 Pr. Nauki, 03028 Kyiv, Ukraine
[2] ICTEAM, Université Catholique de Louvain (UCLouvain), Louvain-la-Neuve, Belgium
[3] National Technical University of Ukraine 'Igor Sikorsky Kyiv Polytechnic Institute', 37 Pr. Peremohy, 03056, Kyiv, Ukraine
[*] Author to whom any correspondence should be addressed.

E-mail: yurigom@workmail.com

Keywords: ZnO, charge transport, bulk traps, polycrystalline thin films

Supplementary material for this article is available online

OPEN ACCESS

RECEIVED
5 November 2024

REVISED
15 December 2024

ACCEPTED FOR PUBLICATION
2 January 2025

PUBLISHED
10 January 2025

Abstract

Kelvin Probe Force Microscopy and Scanning Spreading Resistance Microscopy measurements of hydrogen-doped polycrystalline ZnO films deposited by RF magnetron sputtering with addition of methane have shown that doping of the grain boundaries is higher than that of grains, so that the current flows preferably along the grain boundaries. Current–voltage measurements and admittance spectroscopy of ZnO/n-Si heterostructures were used to assess the density of bulk and interface states in ZnO films with thicknesses of 75 and 135 nm. The charge carrier transport at low temperatures was found to follow space charge limited current mechanism. The density of bulk states is lower in the thicker ZnO film due to the longer passivation effect of hydrogen during deposition.

Introduction

Transparent conductive oxide films are the key elements in many applications including photovoltaic cells, light emitting diodes and touch screens. Polycrystalline zinc oxide (pc-ZnO) is considered now as a potential replacement of indium tin oxide transparent conductive films due to the absence of highly expensive and rare indium and lower production costs. Pc-ZnO has been suggested as an electron-collecting layer for both silicon-based [1, 2] and CIGS-based [3–5] solar cells. Undoped ZnO films have intrinsic *n*-type conductivity, but are too resistive and need to be additionally doped to be used as conductive layers. One of the possible *n*-type dopant is hydrogen which acts as a shallow donor in ZnO [6] and passivates defects at the interfaces and grain boundaries (GBs).

Recently it has been found that addition of methane into working gas during pc-ZnO deposition by RF magnetron sputtering provides an effective *n*-type doping of the pc-ZnO films [7–9]. The *n*-doping in this case was attributed to the incorporation of hydrogen into the ZnO film during plasma assisted deposition process enhancing the formation of shallow donor defects. The analysis of the chemical composition showed also carbon incorporation from methane [7]. The hydrogen concentration in the films deposited with addition of methane was by an order of magnitude higher than in the films deposited with addition of molecular hydrogen and the electrical conductivity was respectively higher [8]. It was shown in [9] that electrical, structural and optical properties of deposited ZnO films depend on the thickness of the film. The conductivity of the film was found to increase considerably with an increase of the film thickness. The grain and subgrain boundaries were found to be the most conductive regions of the doped polycrystalline ZnO film. The higher electrical conductivity of the grain boundaries was attributed to enhanced diffusion of hydrogen dopants through the low-density paths during the deposition process.

In this paper, we study the influence of hydrogen incorporation on the local electronic properties of zinc oxide (ZnO:H) film using Kelvin Probe Force Microscopy (KPFM) and Scanning Spreading Resistance

Microscopy (SSRM). We report also the results of electrical measurements of Ni/ZnO/*n*-Si heterostructures with two different thicknesses of the ZnO layer. Current–voltage measurements and impedance spectroscopy were applied to study the effect of the film thickness on the density of interface states at the ZnO/Si interface and on parameters of the electrically active states in the bulk of the ZnO layer. Based on these results we discuss the possible mechanisms of the carrier flow and the effect of traps on the carrier transport in such heterostructures.

Experimental

The pc-zinc oxide films were deposited by RF (13.56 MHz) magnetron sputtering in 16 sccm argon flow diluted by 4.1 sccm flow of methane at a discharge power of 175 W and a working pressure of 10^{-1} Pa. Further details of the deposition process can be found in [7]. The 140 nm thick ZnO:H film was deposited on a nickel ohmic back contact for scanning probe microscopy measurements. The NanoScope IIIa Dimension 3000™ scanning probe microscope was employed to investigate the nanomorphological and nanoelectrophysical properties of ZnO:H films. Local surface potential mapping was conducted using frequency-modulated KPFM measurements, utilizing platinum-iridium (PtIr) tips with a nominal tip apex radius of 20 nm. A two-path technique was applied, incorporating a lift height of 15 nm to mitigate the effects of surface relief and van der Waals forces. The KPFM tip oscillated on the second path at the drive frequency of 73.6 kHz with an amplitude of 800 mV. The work function of the tips was calibrated using certified highly ordered pyrolytic graphite (HOPG, ZYB Grade). SSRM measurements were executed in contact mode, employing solid platinum tips with a spring constant of 0.3 N m^{-1} and a tip apex radius of less than 20 nm. These measurements were carried out under ambient conditions (23 °C, 40% r.h.). The bias voltages applied were well below those that can cause electrochemical changes such as reducing or localized etching.

The effect of thickness on electrical properties of the films and of the ZnO/Si heterostructures was studied using ZnO:H films with thicknesses of 75 and 135 nm deposited onto the surface of *n*-type silicon wafers (5 Ohm × cm). The top contact to ZnO was formed by deposition of circular Ni dots (1.2 mm diameter) onto the ZnO surface using dc magnetron sputtering. The bottom contact was formed by rubbing Ga/Zn eutectic into the back side of the silicon wafer. Ni as a contact to ZnO was chosen taking into account the closeness of the metal work function and the position of the Fermi level in ZnO to guarantee a good and non-rectifying contact between the metal and the film. The ohmic behavior of the Ni/ZnO contacts was checked by measuring *I-V* characteristics of the Ni/ZnO/Ni structures which were found linear [10]. Finally, we obtained the ZnO/*n*-Si heterostructure with Ni contact dots at the surface of the ZnO film. The Ni/ZnO/*n*-Si heterostructures were characterized by *I-V* measurements and impedance spectroscopy. *I-V* characteristics were measured by a Keithley 6485 picoammeter, conductance—frequency (*G-f*) and capacitance-frequency (*C-f*) characteristics were measured in the frequency range from 100 Hz to 1 MHz by an Agilent 4284 LCR meter.

Results and discussion

Surface potential and local resistance of ZnO film from KPFM and SSRM

In our study of hydrogen-doped zinc oxide (ZnO:H) films through Kelvin Probe Force Microscopy and Scanning Spreading Resistance Microscopy, we have elucidated several critical aspects of hydrogen incorporation, which are important for understanding of the physical mechanisms responsible for the electrical properties of the studied ZnO films. Special attention is paid to elucidating such aspects as conductivity across grain boundaries and the position of the Fermi level in the grain and grain boundary regions.

The surface morphology of the ZnO:H film under investigation is presented in figure 1(a). This surface exhibits a granular structure, with grain sizes varying between 50 and 300 nm and featuring a root mean square (RMS) roughness of 11 nm. A statistical analysis of the grain sizes reveals an average size of 190 nm, accompanied by a standard deviation of 58 nm. Furthermore, the grains are densely packed and possess well-defined boundaries, albeit lacking crystallographically defined geometric features.

For better understanding of the electronic properties of the ZnO film, the contact potential difference (CPD) along the film surface was assessed using KPFM. This measurement technique allows evaluating the local difference in work function through the contact potential difference (CPD) between the platinum tip and the hydrogen-doped zinc oxide surface. The physical origin of CPD formation in such experiments is explained and illustrated in [11]. The work function of *n*-ZnO consists of the ZnO electron affinity (4.45 eV) plus the depth of the Fermi level position in the ZnO band gap measured from the conduction band bottom. In our case, with the impurity concentration measured by Hall effect measurements of around 10^{20} cm^{-3} [9], the Fermi level in *n*–ZnO is situated near the conduction band edge, so the work function is equal to the electron affinity of ZnO. If the local carrier concentration at some point at the surface is lower, the Fermi level shifts down into the band gap and the respective work function becomes larger. Since the work function of the PtIr tip (5.5 eV) is higher than

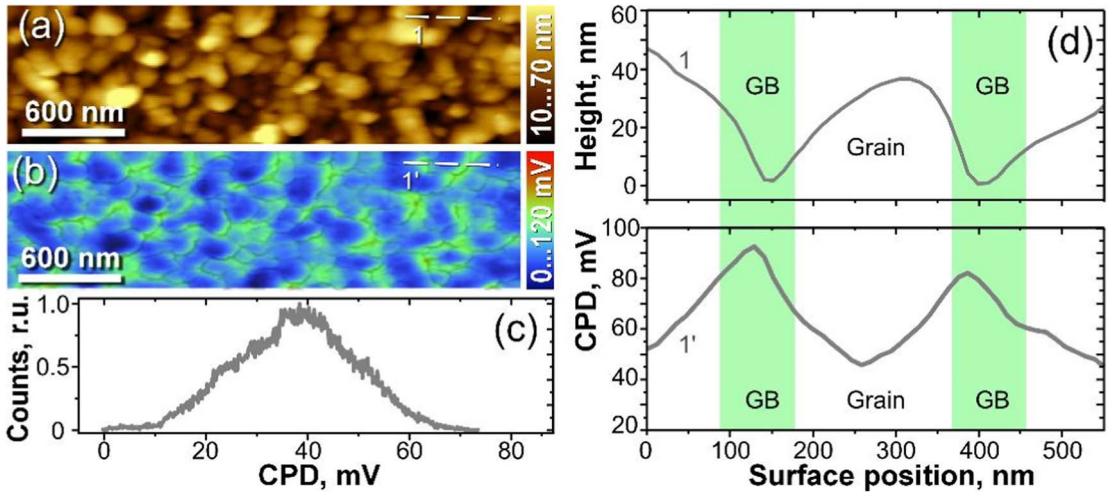

Figure 1. (a) Surface morphology and (b) corresponding KPFM images of the hydrogen-doped zinc oxide film obtained by RF magnetron sputtering in a methane ambient. (c) Histogram of the CPD for the fragment shown in (b). (d) Profiles of individual grain height (1) and CPD (1') along the dashed line indicated in (a) and (b). The areas marked as GB patches indicate the locations of grain boundaries. Grain boundaries are shown in (b) for visualization purposes.

the electron affinity of ZnO, the measured CPD is higher in the regions with the higher impurity concentration. Therefore, the CPD map reflects the distribution of the charge carrier concentration over the surface of the semiconductor.

Figure 1(b) shows the KPFM image of the ZnO film surface, and the histogram of the CPD for the respective fragment is shown in figure 1(c). Figure 1(d) presents profiles of individual grain height (*1*) and CPD (*1′*) along the dashed lines indicated in figures 1(a) and (b). The green areas in figure 1(d) correspond to the locations of grain boundaries. A reduced CPD between the tip and the grain, relative to that at the grain boundary (curve 1'), indicates that the Fermi level is closer to the conduction band edge at the grain boundaries. This means that the carrier concentration at these boundaries is higher than in the grains due to a higher density of hydrogen-related donor centers.

The observed grain boundary-related CPD effects align with the peculiarities of local resistivity identified through SSRM measurements. By analyzing the local spreading resistance map presented in figure 2(b) and the corresponding cross sections of relief (figure 2(a)) and resistance depicted in figure 2(d), local resistivity ρ values can be estimated using the formula as $\rho = 4aR$, where a represents the SSRM tip apex radius and R denotes resistance [12, 13]. The grain boundaries exhibit significantly lower resistivity (approximately 0.02 Ω·cm) compared to the grains (approximately 8 Ω·cm), as shown in figure 2(d). The resistivity values of individual grains and grain boundaries, extended through statistical analysis over the entire surface fragment, are presented in the histogram (figure 2(c)). These results indicate that hydrogen doping has notably enhanced conductivity at the grain boundaries.

The increase in conductivity in the grain boundary regions can be attributed to stronger hydrogen segregation at the grain boundaries, resulting in a higher concentration of interstitial hydrogen (H_i) and complexes consisting of an oxygen vacancy and hydrogen (H_O), which according to the theoretical studies [6], act in ZnO as shallow donors and thus elevate the local electron density. It is logical to expect that the coefficient of diffusion of hydrogen through grain boundary is higher than through bulk of the grains due to lower density of the material in this location, so that hydrogen flow through GB dominates over flow through the bulk of grains. Moreover, more defective structure in grain boundaries promotes more concentration of trapping sites, which in combination with high hydrogen flow results in high concentration of hydrogen trapped in grain boundaries.

Besides, hydrogen segregated at the grain boundaries can also passivate dangling bonds and defects which create deep level states in the ZnO band gap, thereby reducing recombination and defect-related scattering and further increasing conductivity in the grain boundary regions.

The observed significantly lower resistivity at the grain boundaries compared to the grains presents a notable deviation from the conventional understanding on the conductivity of the polycrystalline semiconductors, wherein grain boundaries are typically viewed as barriers to the charge carrier transport [14–16].

Density of traps from forward *I-V* characteristics of ZnO/*n*-Si heterostructure

It was shown in [9] that ZnO films synthesized by magnetron sputtering in argon/methane ambient possess a high *n*-type doping with the carrier concentration of the order of 10^{20} cm^{-3}. In this case, the Fermi level is situated near the bottom of the conduction band of ZnO. Taking into account the difference in electron affinity

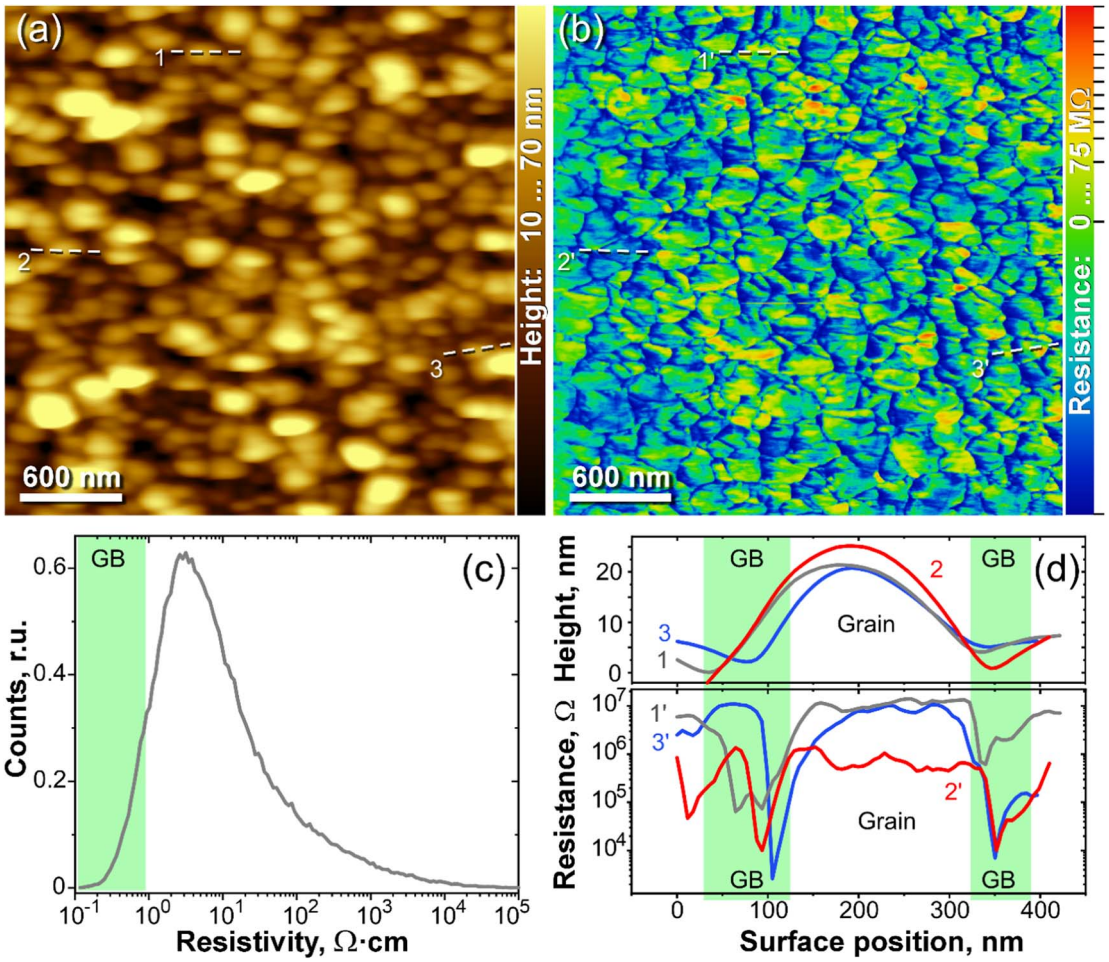

Figure 2. (a) Surface morphology and (b) corresponding SSRM images of the surface of a hydrogen-doped zinc oxide film, obtained with a -0.4 V DC sample bias. (c) Resistivity histogram as estimated from (b). (d) Profiles of individual grain height and resistance along the dashed lines indicated in (a) and (b). Curves 1, 2 and 3 and 1', 2' and 3' in (d) correspond to respective dashed lines in (a) and (b). The areas labeled as GB patches denote the grain boundaries.

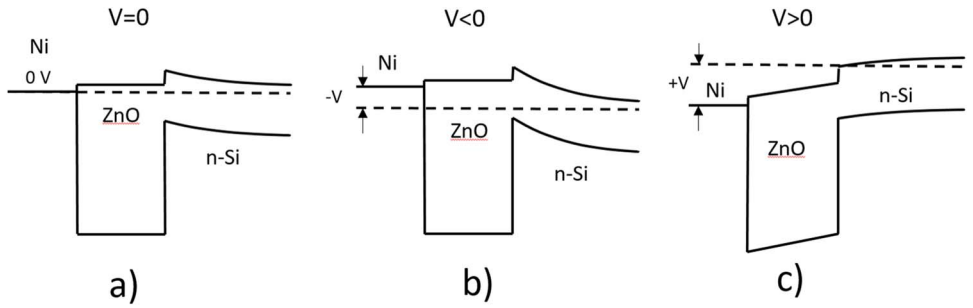

Figure 3. Band diagrams of Ni/ZnO/*n*-Si heterostructure (a) in equilibrium, (b) under the negative or (c) positive bias.

for ZnO (4.45 eV) and Si (4.05 eV) and the respective band gap values, we can draw the band diagrams for the *n*-ZnO/*n*-Si heterostructure for zero, negative and positive bias at the metal electrode (figure 3). It can be seen that the isotype *n*-ZnO/*n*-Si heterojunction forms type-II (staggered) junction with the conduction band offset of 0.4 eV at the interface. Silicon wafers used in the experiment have donor concentration 10^{15} cm^{-3}. At temperature 300 K the Fermi level is situated at E_c-0.26 eV. Since the Fermi level in highly doped ZnO is situated at the conduction band bottom, the band bending in silicon in this case is equal to the difference between the band offset and the depth of the Fermi level in silicon, i.e. 0.14 eV.

The current–voltage (*I-V*) characteristics of the Ni/ZnO/*n*-Si heterostructures (see figure 4(a)) measured at 300 K show an evident asymmetry due to a potential barrier existing at the ZnO/*n*-Si interface. Figure 4(b)

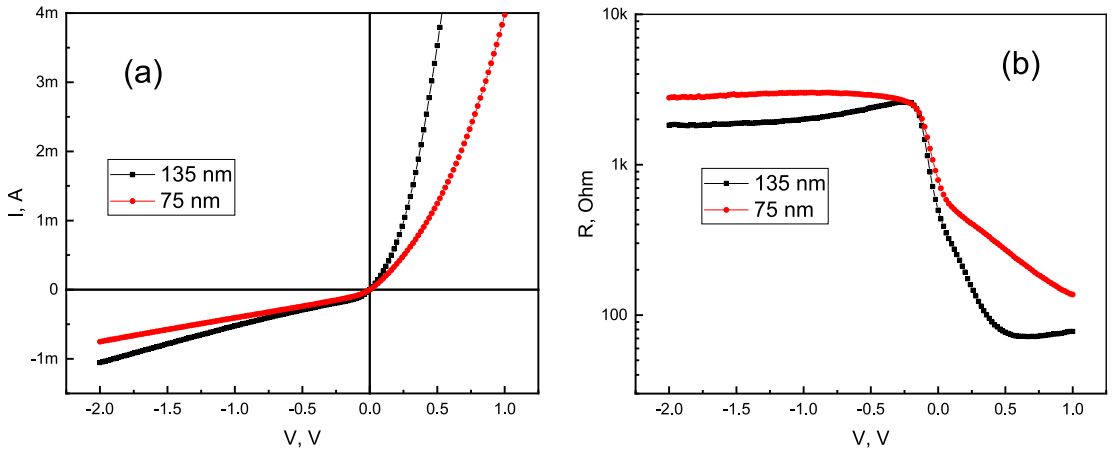

Figure 4. (a) *I-V* characteristics of the Ni/ZnO/*n*-Si heterostructures with different thickness of the ZnO layer. (b) Voltage dependences of the resistance of the Ni/ZnO/*n*-Si heterostructures.

shows the resistance of the heterostructures with different thickness obtained by differentiation of *I-V* characteristics. At a positive voltage at the metal contact the effect of the silicon depletion layer on electrical characteristics is eliminated, because the potential barrier in silicon is flattened. In this case the total resistance of the heterostructure is the sum of resistances of the ZnO layer, contacts and the silicon bulk. Since two last contributions are the same for both samples, the differences in the total resistance are ascribed to the different resistance of the ZnO layer. At the forward bias ($V = +1.0$ V) the resistance of the heterostructure is 137 Ohm for 75 nm film and 78 Ohm for 135 nm film. It can be seen that the resistance of the film at room temperature increases with decreasing of the thickness, which is consistent with the results reported in [9].

Measurements of current–voltage characteristics at low temperatures were used to clarify the mechanism of charge carrier transport through the heterostructure. At low forward voltages ($V < +0.2$ V) the current is controlled by the thermionic emission over the barrier at the interface. However, this barrier is being flattened with an increase of the forward voltage, and other limiting factors come into play. Among several possible mechanisms that have been suggested to describe the transport in heterostructures and thin polycrystalline films, we can mention the following: trap assisted tunneling (TAT) [17], variable range hopping (VRH) [18], multitunneling capture-emission (MTCE) [19] and space charge-limited currents (SCLC) [20–22].

In our case the problem of determination of the prevailing transport mechanism is rather complicated because the pc-ZnO film, which mainly determines the resistivity of the structure at a forward bias, consists of grains separated by grain boundaries [9]. It was mentioned earlier, that the current in pc-ZnO films doped using methane flows predominantly along the grain boundaries and sub-grain boundaries. This is explained by non-uniform doping of the ZnO polycrystalline film with hydrogen during the deposition process. Hydrogen with its extremely high diffusivity easily penetrates along the grain boundaries into the depth of the film and causes additional doping of the grain surfaces. The resistance measured between the probe and the metal substrate for two adjacent points at the surface of ZnO film can differ by three orders of magnitude, depending on whether the probe is touching the grain or grain boundary (see figure 2 (b, d)). In this case the picture is quite different from the generally accepted concept describing the transport in polycrystalline materials as taking place through highly conductive grains separated by potential barriers (see figure 5(a)). In our ZnO films, we have instead highly conductive grain boundaries covering less conductive grains and the current flows along the potential valleys in grain boundaries as illustrated in figure 5(b). Taking the above mentioned arguments into account, the band diagrams presented in figure 3 should be considered as purely illustrative, because the Fermi level at the surface of the granular ZnO film can change its position depending on the actual doping at the microscopic scale.

Figure 6 shows the forward branches of *I-V* characteristics for two Ni/ZnO/*n*-Si samples with different ZnO thickness measured at temperatures 150, 180, 210 and 240 K and plotted in double logarithmic coordinates. One can see that they look similar to the dependences typical for SCLC transport. Such a mechanism of carrier transport can be applied to our samples since our heterojunctions are isotype, and we observe the single-carrier (electron) transport. Comprehensive reviews on SCLC in semiconductors can be found in recent papers [22, 23] though the history of the problem goes back to the middle of the last century [24–26]. According to the theory of SCLC the initial, low-voltage section of *I-V* curves exhibit Ohmic conduction with the linear dependence on *V*. If a semiconductor contains traps, the second part of the *I-V* characteristic is observed with the critical exponent $m > 2$ of the power law dependence $I \sim V^m$. This part is usually called as a region with trap-filled limited current. Most often the distribution of traps in the band gap of an *n*-type semiconductor is assumed in the form of

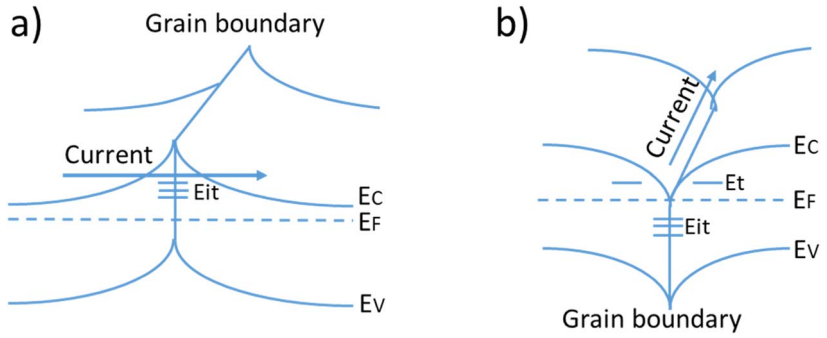

Figure 5. Band diagrams and current flow directions (a) for the potential barrier and (b) for the potential valley at the grain boundary.

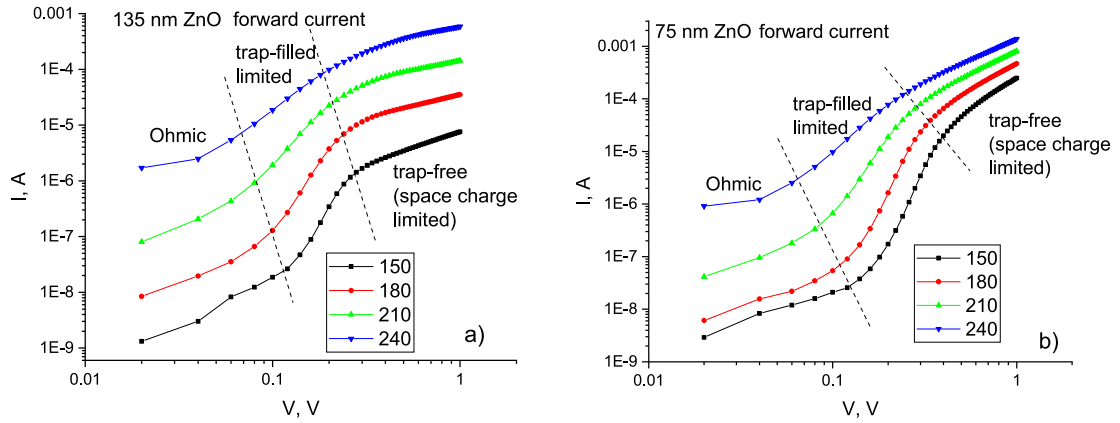

Figure 6. Forward branches of *I-V* dependences for Ni/ZnO/*n*-Si heterostructure (a) with 135 nm and (b) 75 nm thick ZnO layer.

exponential tail near the edge of the conduction band [22]:

$$D_t = \frac{N_t}{E_t}\exp\left(\frac{E}{E_t}\right), \tag{1}$$

where N_t is the trap concentration, E_t is the characteristic energy and E is the energy measured from the bottom of the conduction band. It can be seen from equation (1) that E_t represents here not the depth of the local defect level in the forbidden band, but it is the factor determining the width of the exponential defect band tail near the conduction band edge. N_t is the concentration of traps per volume unit at the bottom of the conduction band.

At a higher voltage the log(I) versus log(V) dependence shows the transition to the region with $m = 2$, which is called trap-free or space-charge limited current. The maximum value m^* of the critical exponent m in the trap-filled limited region is connected with the characteristic energy E_t by the equation [22]:

$$E_t = (m^* - 1)\cdot kT, \tag{2}$$

here T is the measurement temperature.

The concentration of traps N_t can be found if the voltage V_{tc} is known, at which the transition from the second to the third part of the dependence is observed, from the equation [25]:

$$N_t = \frac{l}{l+1}\left(\frac{\varepsilon V_{tc}}{qd^2}\right)^{\frac{l-1}{l}}\left[\frac{8N_c}{9}\left(\frac{2l+1}{l+1}\right)^{l+1}\right]^{1/l} \tag{3}$$

where $l = m^*-1$, ε is the film permittivity, d is the film thickness, N_c is the effective density of states in the conduction band of the semiconductor.

Figure 7 shows the temperature dependences of trap concentration N_t and characteristic energy E_t for two samples with different thickness of ZnO layer. It can be seen that at lower temperatures the thinner film is characterized by substantially higher concentration of traps, which are extended deeper into the band gap. The difference in N_t can be explained by the fact that the deposition time for 135 nm ZnO film is approximately twice longer than for 75 nm film. During all this time hydrogen penetrates inside the film along the grain boundaries and effectively passivates the defects spatially situated in the near-surface layer of the grains.

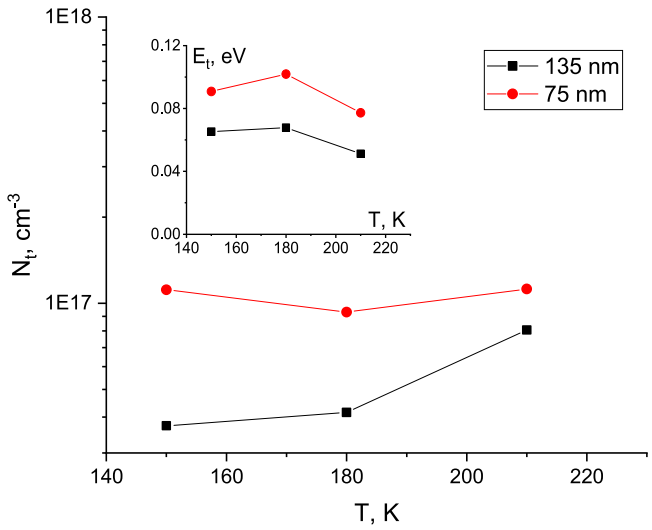

Figure 7. Concentration of traps N_t as a function of temperature for two Ni/ZnO/*n*-Si heterostructures with different thickness of ZnO layer. Inset shows the dependence of the characteristic energy E_t.

Considering the carrier transport through the ZnO film, we must take into account different flow paths for the carriers and different limiting factors for the carrier flow. Evidently, at low voltages the main contribution into the current comes from the transport via the highly conductive paths along the grain boundaries and sub-grain boundaries. However, these paths are narrow, and with an increasing voltage they fail to transport an increasing flux of carriers, so the near-surface regions of ZnO film with lower doping level start to control the current at higher voltages. In addition, the charge captured in the traps near the conducting paths can partially block the charge transfer through these paths, making the near-surface layers of ZnO grains the decisive factor in the carrier transport.

Interface and bulk states from admittance spectroscopy of ZnO/*n*-Si heterostructure

Admittance spectroscopy (measurement of ac conductance G and capacitance C as a function of frequency f) is widely and effectively used for assessment of defect parameters in *p-n* junctions [27], heterojunctions [28], Schottky diodes [29] and MIS capacitors [30]. In a standard approach of Nicollian and Goetzberger $G(f)/\omega$ ($\omega = 2\pi f$) curves for a given bias V exhibit a maximum $(G/\omega)_{max}$ at some characteristic frequency f_0 [31]. The value of $(G/\omega)_{max}$ is proportional to the number of electron states contributing to the charging/recharging process. The density of states D_{it} is then determined from the equation

$$D_{it} = \frac{2.5 \cdot (G/\omega)_{max}}{q \cdot A}, \tag{4}$$

where q is the elementary charge and A is the sample area. The problem is that the conductance peak may be attributed to response of the trap centers both at the interface between different materials and within the semiconductor bulk, and in a general case it is not easy to distinguish between these two options. Another problem, which is actual for heterojunctions and for the MIS structures with leaky dielectrics, is the necessity to get rid of a leakage current which contributes to the trap-related ac signal and distorts the G/ω curve, especially in the range of low measurement frequencies. In the case of leaky dielectric layers or heterostructures, the $G(f)$ curves needs in correction, as described in [28, 32]. Before the conductance related to interface traps is plotted in G/ω versus frequency coordinates, the parasitic dc conductance should be subtracted from the measured value. The value of the dc conductance G_{DC} for a given bias can be determined by differentiation of the current–voltage dependences.

It is known from the theory of admittance spectroscopy that the measured values of C and G, which are related to imaginary and real components of the complex admittance, are connected with Kramers-Kronig relations [33]. This allows to replace the value of G/ω with the magnitude $-f\frac{dC}{df}$, which is called loss factor [34], and can be easily calculated from the $C(f)$ dependences using differentiation. In this case there is no need to subtract a parasitic leakage conductance from the measured data.

The third approach to the interpretation of the ac measurements was suggested by Brus [35, 36], when the values of G are calculated from the values of measured real R and imaginary X components of the complex impedance Z by the equation:

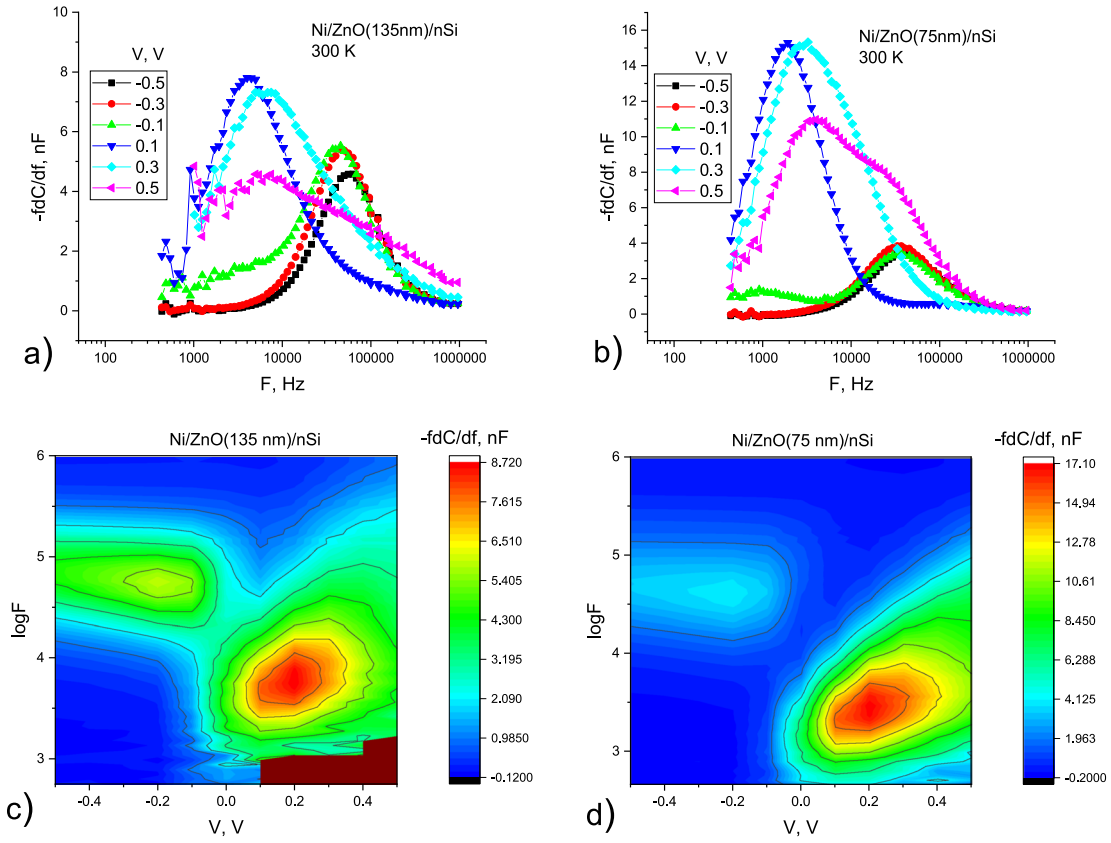

Figure 8. (a), (b) Dependences of the loss factor on frequency for different applied voltages and (c), (d) loss maps for (a), (c) 135 nm and (b), (d) 75 nm thick ZnO film.

$$G = \frac{R - R_c}{(R - R_c)^2 + X^2} - \frac{1}{R_{sh}}, \tag{5}$$

where R_c is the contact resistance, equal to the resistance at the highest frequency, and R_{sh} is the shunt resistance, equal to the resistance of the low-frequency end of the experimental $-X$ versus R dependences (see Supplementary Material, Fig. S1).

Standard LCR meters initially measure the amplitude and the phase shift of the output ac signal in respect to the input one, and then recalculate the results in the form of (C,G) versus f or (X, R) versus f dependences. The choice of one of the three above-mentioned methods for estimation of the density of states in the structure under study depends on signal-to-noise ratio in various frequency ranges, the presence of parasitic interferences due to contact resistance or inductivity of connection cables, clarity of resulting plots, etc.

Figure 8 shows the results of admittance measurements in two different presentations. Figures 8(a), (b) show the dependences of $-f\frac{dC}{df}$ on frequency for different biases. Figures 8(c), (d) are the loss maps in which the color reflects the amplitude of the signal in dependence on frequency (vertical axis) and applied voltage (horizontal axis). From the loss map it becomes evident that there are at least two different types of electrically active centers that give a response to the testing signal. The interface states are known to be energetically situated within the band gap. The maximum contribution of these states into dissipation is observed when they are half-empty, that is, when the Fermi level crosses their position on the energy scale. From the band diagrams it is clear, that this may occur only at a negative bias at the metal electrode, when the silicon surface is turned into the depletion mode. Therefore, it is reasonable to assign the left-hand spot at the map to the response of the states spatially located at the ZnO/Si interface, or in the SiO_x transition layer. The right-hand spot with higher amplitude is observed at positive biases. In this case all interface traps are filled and do not contribute into the recharging process. Therefore, we attribute the respective ac response to the defect electrically active centers spatially situated in the bulk of ZnO film.

Equation (4) was applied to calculate the density of interface states from the maximum values of the $-f\frac{dC}{df}$ curves for the interface related peaks in the voltage range where these peaks are manifested, i.e. at negative biases. D_{it} as a function of applied voltage is plotted in figure 9(a). If we assume that the bulk states are uniformly distributed inside the ZnO film, their density D_t can be roughly estimated by division of the maximum value of

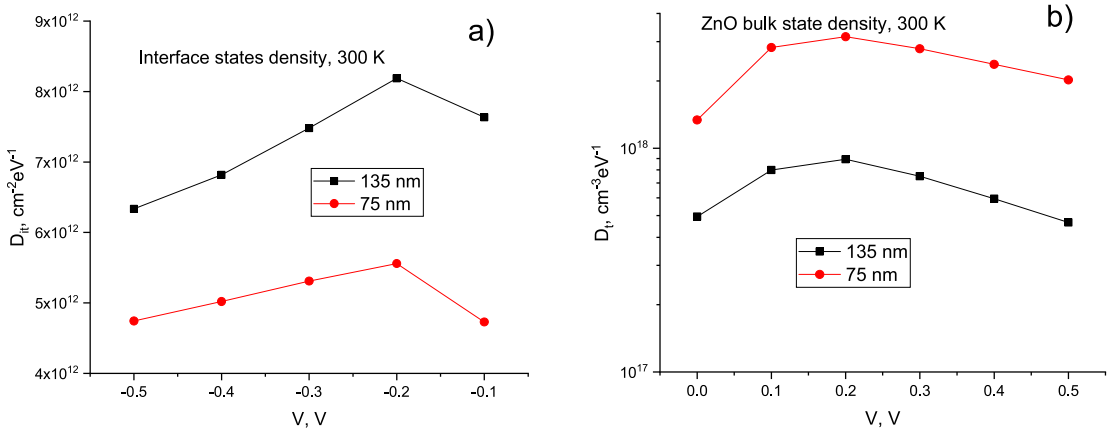

Figure 9. Dependences of (a) interface states density and (b) bulk trap density for two Ni/ZnO/*n*-Si heterostructures with different thickness of ZnO layer.

$-f\frac{dC}{df}$ versus f dependences by the thickness of the film. Respective dependences of D_t on the applied bias are plotted in figure 9(b).

It can be seen that the sample with the thicker film has slightly higher (by a factor of 1.5) density of interface states, but significantly lower (by a factor of 4) density of bulk traps.

The maximum of the bulk related peak of $-f\frac{dC}{df}$ versus f dependences is observed at the forward voltage +0.2 V. At the same voltage, as one can see from figure 6, the SCLC trap-filled mode is observed in dc *I-V* characteristics at low temperatures. The ZnO bulk trap concentrations per volume unit extracted from SCLC measurements at 180 K were 4.2×10^{16} cm^{-3} and 9.3×10^{16} cm^{-3} for 135 nm and 75 nm film, respectively (figure 7). Recalculation of the bulk trap density obtained from admittance measurements at +0.2 V (figure 9(b)) into the trap concentration per volume unit gives us the values of 4.5×10^{16} cm^{-3} and 1.5×10^{17} cm^{-3} for 135 nm and 75 nm film, respectively, which are close to those obtained from SCLC. Therefore, we can conclude that by different measurement technique we detect the same electrically active centers, which are manifested either in dc current at low temperatures, or at room temperature in ac mode. This is also supported by the fact that the admittance response corresponding to shallower traps in the 135 nm thick film (see inset in figure 7) are registered at higher frequency (5455 Hz, compared to the 2608 Hz for 75 nm thick film). The effect of hydrogen during the magnetron deposition of ZnO films using methane consists, first, in doping of grain boundaries and sub-grain boundaries and, second, in annealing of the defect centers spatially located in the near-surface regions of grains and energetically situated at about 0.1 eV below the bottom of the conduction band.

Conclusions

In conclusion, we have studied the electrical characteristics of traps in Ni/ZnO/*n*-Si heterostructures with ZnO layers deposited by magnetron sputtering in a methane ambient. Addition of methane was found to provide high but severely non-uniform hydrogen doping with enhanced electrical conductivity of grain and sub-grain boundaries. Measurements were carried out in the samples with two different thicknesses of the ZnO layer (135 and 75 nm). Admittance measurements have shown that the density of bulk states in ZnO layer is lower in the thicker film due to the longer passivation effect of hydrogen during deposition. The charge carrier transport at low temperatures was found to follow SCLC mechanism. The density of states responsible for the dc transport at low temperatures is lower in the thicker film as well.

Acknowledgments

The work was (partially) supported by the Ministry of Education and Science of Ukraine in the frame of the joint research programs of Ukraine and Czech Republic (project #M/22-2022) and in the frame of the research project #M/88-2024, and by the Program Science for Peace and Security (NATO project SPS G5853).

Data availability statement

All data that support the findings of this study are included within the article (and any supplementary files).

ORCID iDs

Y V Gomeniuk https://orcid.org/0000-0001-9999-5957
A V Vasin https://orcid.org/0000-0003-2771-0670

References

[1] Ding J, Zhou Y, Dong G, Liu M, Yu D and Liu F 2017 Solution-processed ZnO as the efficient passivation and electron selective layer of silicon solar cells *Prog. Photovoltaics Res. Appl.* **26** 974
[2] Romero R, López M C, Leinen D, Martin F and Ramos-Barrado J R 2004 Electrical properties of the n-ZnO/c-Si heterojunction prepared by chemical spray pyrolysis *Mater. Sci. Eng.* B **110** 87
[3] Paul S, Lopez R, Repins I L and Li J V 2018 Study of charge transport properties in a ZnO/CdS/Cu(In,Ga)Se_2 solar cell via admittance spectroscopy *J. Vac. Sci. Technol.* B **36** 022904
[4] Yeh C L, Hsu H R, Chen S H and Liu Y 2012 Near infrared enhancement in CIGS-based solar cells utilizing a ZnO:H window layer *Opt. Express* **20** A806
[5] Choi E C, Cha J H, Jung D Y and Hong B 2016 Structural, electrical and optical properties of ZnO film used as a buffer layer for CIGS thin-film solar cells *Journ. Nanosci. Nanotechnol.* **16** 5087
[6] Van de Walle C G 2000 Hydrogen as a cause of doping in zinc oxide *Phys. Rev. Lett.* **85** 1012
[7] Vasin A V *et al* 2020 Methane as a novel doping precursor for deposition of highly conductive ZnO thin films by magnetron sputtering *Vacuum* **174** 109199
[8] Vasin A V *et al* 2022 On the nature of doping effect of methane in ZnO thin films deposited by RF-magnetron sputtering *J. Mater. Sci., Mater. Electron.* **33** 6421
[9] Vasin A V *et al* 2024 Structural insight into nanoscale inhomogeneity of electrical properties in highly conductive polycrystalline ZnO thin films doped using methane *J. Phys. D: Appl. Phys.* **57** 155101
[10] Gomeniuk Y V *et al* 2023 Effect of PEDOT:PSS layer deposition on electrical and photoelectrical properties of n^+-ZnO/n-Si heterostructure *J. Electron. Mater.* **52** 3112
[11] Melitz W, Shen J, Kummel A C and Lee S 2011 Kelvin probe force microscopy and its application *Surf. Sci. Reports* **66** 1
[12] Clarysse T and Vandervorst W 2000 Qualification of spreading resistance probe operations *I. J. Vac. Sci. Technol.* B **18** 369
[13] Clarysse T and Vandervorst W 2000 Qualification of spreading resistance probe operations *II. J. Vac. Sci. Technol.* B **18** 381
[14] Seto J Y W 1975 The electrical properties of polycrystalline silicon films *Journ. Appl. Phys.* **46** 5247
[15] Kumar M, Basu T and Som T 2016 Local probe microscopic studies on Al-doped ZnO: Pseudoferroelectricity and band bending at grain boundaries *Journ. Appl. Phys.* **119** 014307
[16] Gonzalez-Julian J, Neuhaus K, Bernemann M, Pereira da Silva J, Laptev A, Bram M and Guillon O 2018 Unveiling the mechanisms of cold sintering of ZnO at 250 °C by varying applied stress and characterizing grain boundaries by kelvin probe force microscopy *Acta Materiala* **144** 116
[17] Kim H, Choi S and Choi B J 2020 Influence of AlN and GaN pulse ratios in thermal atomic layer deposited AlGaN on the electrical properties of AlGaN/GaN Schottky diodes *Coatings* **10** 489
[18] Huang Y-L, Chiu S P, Zhu Z-X, Li Z-Q and Lin J-J 2010 Variable-range-hopping conduction processes in oxygen deficient polycrystalline ZnO films *J. Appl. Phys.* **107** 063715
[19] Płaczek-Popko E, Paradowska K M, Pietrzyk M A and Kozanecki A 2017 Carrier transport mechanisms in the ZnO based heterojunctions grown by MBE *Opto-Electron. Rev.* **25** 181
[20] Dongaonkar S *et al* 2010 Universality of non-ohmic shunt leakage in thin-film solar cells *J. Appl. Phys.* **108** 124509
[21] Williams B L, Smit S, Kniknie B J, Bakker K J, Keuning W, Kessels W M M, Schropp R E I and Creatore M 2015 Identifying parasitic current pathways in CIGS solar cells by modelling dark J–V response *Prog. Photovolt: Res. Appl.* **23** 1516
[22] Röhr J A, Moia D, Haque S A, Kirchartz T and Nelson J 2018 Exploring the validity and limitations of the Mott–Gurney law for charge-carrier mobility determination of semiconducting thin-films *J. Phys: Condens. Matter* **30** 105901
[23] Zhang P, Ang Y S, Garner A L, Valfells Á, Luginsland J W and Ang L K 2021 Space–charge limited current in nanodiodes: ballistic, collisional, and dynamical effects *J. Appl. Phys.* **129** 100902
[24] Mott N F and Gurney R W 1950 *Electronic Processes in Ionic Crystals* (Oxford Univ. Press)
[25] Mark P and Helfrich W 1962 Space-charge-limited currents in organic crystals *J. Appl. Phys.* **33** 205
[26] Lampert M A 1964 Volume-controlled current injection in insulators *Rep. Prog. Phys.* **27** 329
[27] Derdouri M, Mahdjoubi L and Benmalek M 1982 Analysis of admittance spectroscopy method for the study of deep levels *Solid State Electron.* **25** 925
[28] Walter T, Herberholz R, Müller C and Schock H W 1996 Determination of defect distributions from admittance measurements and application to Cu(InGa)Se_2 based heterojunctions *J. Appl. Phys.* **80** 4411
[29] Vincent G, Bois D and Pinard P 1975 Conductance and capacitance studies in GaP Schottky barriers *J. Appl. Phys.* **46** 5173
[30] Casey H C Jr, Cho A Y, Lang D V and Nicollian E H 1978 Measurement of MIS capacitors with oxygen-doped AlxGa1-xAs insulating layers on GaAs *J. Vac. Sci. Technol.* **15** 1408
[31] Nicollian E H and Bruce J R 1982 *MOS Physics and Technology* (Wiley)
[32] Gomeniuk Y, Nazarov A, Vovk Y, Lu Y, Buiu O, Hall S, Efavi J K and Lemme M C 2006 Low-temperature conductance measurements of surface states in HfO_2-Si structures with different gate materials *Mater. Sci. Semicond. Process.* **9** 980
[33] von Hauf E 2019 Impedance spectroscopy for emerging photovoltaics *J. Phys. Chem.* C **123** 11329
[34] Parion J, Scaffidi R, Flandre D, Brammertz G and Vermang B 2023 Low-temperature admittance spectroscopy for defect characterization in Cu(In,Ga)(S,Se)2 thin-film solar cells *IEEE EUROCON 2023 - 20th Int. Conf. on Smart Technologies* 99–104
[35] Brus V V 2012 On impedance spectroscopy of nonideal heterojunctions *Semicond. Sci. Technol.* **27** 035024
[36] Brus V V 2013 The effect of interface state continuum on the impedance spectroscopy of semiconductor heterostructures *Semicond. Sci. Technol.* **28** 025013